Field Emission and RF Breakdown in High-Gradient Room-Temperature Linac Structures[*]

J. W. Wang and G. A. Loew

Stanford Linear Accelerator Center, Stanford University, Stanford, CA 94309

*Article based on lecture given at the US-CERN-JAPAN Joint Accelerator School
Hayama and KEK, Japan
September 9-17, 1996*

Field Emission and RF Breakdown in High-Gradient Room-Temperature Linac Structures[a]

J. W. Wang and G. A. Loew

Stanford Linear Accelerator Center, Stanford University,
Stanford, CA 94039, USA

1   Introduction

The purpose of this article is to serve as a tutorial review on the subject of field emission and rf breakdown in high-gradient room-temperature accelerator structures and associated devices. The need to understand and control these two phenomena has become increasingly important because of the prospect of using high-gradient structures in future linear colliders. Electron field emission creates so-called "dark current" which parasitically absorbs rf energy, causes radiation, backgrounds, and possibly wakefields; it seems to be the precursor of rf breakdown, possibly in combination with local outgassing and plasma formation. In turn, rf breakdown limits the operation of accelerators and can cause irreversible damage to their physical structures. Research on these topics is interesting and challenging because it involves a mixture of disciplines such as surface physics, metallurgy, fabrication technologies, microwaves, beam dynamics and plasmas.

Our review consists of four parts:

- Field emission under dc, enhanced and rf conditions

- Experimental set-ups

- Prebreakdown stage: dark current and radiation

- Experimental observations and analysis of rf breakdown

The review ends with conclusions and an outline of work that remains to be done.

2 Field Emission

An understanding of electron field emission (FE) is a prerequisite to discussing prebreakdown and breakdown phenomena. In this section, we review the Fowler-Nordheim equations for electron field emission under dc, enhanced (EFE) and rf conditions.

2.1 DC Field Electron Emission from Ideal Metal Surface

Following Sommerfeld, Fowler and Nordheim calculated the quantum mechanical tunneling of conduction electrons through a modified potential barrier at an ideal, perfectly clean, flat metal surface in an applied electric field.[1, 2] The actual mathematical derivation is briefly outlined below. The one-dimensional potential barrier is illustrated in Figure 1. The effective potential energy $V(z)$ is

$$V(z) = \begin{cases} -W_a & \text{where } z < 0 \\ -eEz - e^2/4z & \text{where } z > 0 \end{cases}, \tag{1}$$

where the term $-e^2/4z$ is the contribution of the interaction of the emitted electron with its image charge and $-W_a$ is the potential energy of the electron when it is inside the metal.
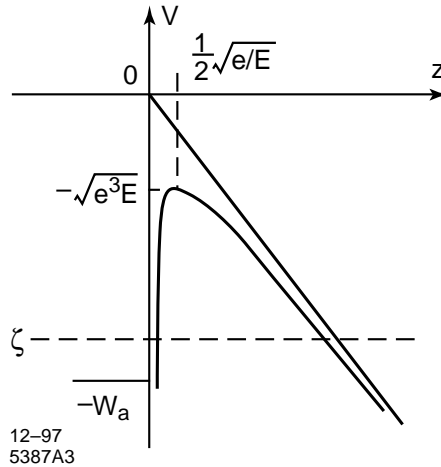

12–97
5387A3

Figure 1: Potential energy diagram showing the modified electric field potential barrier at the boundary of a perfect conductor.

Fowler and Nordheim assumed that the conduction electrons in the metal form a gas of free particles which obey Fermi-Dirac statistics. The number of

electrons within a volume v and with momenta within the range $dP_x dP_y dP_z$ can be expressed by

$$dn = \frac{2v}{h^3} \frac{dP_x dP_y dP_z}{e^{(\mathcal{E}-\zeta)/kT} + 1} \quad , \tag{2}$$

where h is Planck's constant, k is Boltzmann's constant, ζ is called the Fermi energy, $\mathcal{E}$ is the total energy and T is the temperature. The flux of electrons that have normal energy components between W_z and $W_z + dW_z$ and are incident upon the barrier at the surface of the metal is $N(W_z)dW_z$, where $N(W_z)$ is the supply function which can be found by integrating Eq. (2) over all P_x and P_y. The probability $D(W_z)$ of an electron tunneling through the barrier is called the transmission coefficient. Using the WKB approximation, the solution for the time-independent Schrödinger equation yields

$$D(W_z) = \exp\left[-\int_{z_1}^{z_2} \sqrt{\frac{8m}{\hbar^2}[V(z) - W(z)]} dz \right] \quad , \tag{3}$$

where z_1 and z_2 are the zeros of the radicand. The total number of electrons that tunnel through the barrier is obtained by integrating the expression $N(W_z)D(W_z)dW_z$ over all energies. Ordinarily, the lowest energy $-W_a$ is far below the Fermi energy. By setting this limit to $-\infty$, the field emission current density j_F can be obtained:

$$j_F = e \int_{-\infty}^{\zeta} D(W_z)N(W_z)dW_z \quad . \tag{4}$$

For low temperature $(T \leq 300°\text{K})$, it has the form

$$j_F = \frac{1.54 \times 10^{-6} \ E^2}{\phi \ t^2(s)} \ \exp\left[\frac{-6.83 \times 10^9 \ \phi^{1.5}v(s)}{E}\right] \ (\text{A/m}^2) \quad , \tag{5}$$

where E is the surface electric field in V/m, ϕ is the work function of the emitting material in eV, $t(s)$ and $v(s)$ are tabulated dimensionless elliptic functions, and

$$s = 3.79 \times 10^{-5} \ E^{0.5}/\phi \quad , \tag{6}$$

$$v(s) = 0.956 - 1.062 \ s^2 \quad . \tag{7}$$

By substituting these into (5) and letting $t(s) \approx 1$, the Fowler-Nordheim equation takes the following form:

$$j_F = \frac{1.54 \times 10^{-6} \times 10^{4.52\phi^{-0.5}} E^2}{\phi} \ \exp\left(-\frac{6.53 \times 10^9 \phi^{1.5}}{E}\right) \ (\text{A/m}^2) . \tag{8}$$

2.2 Enhanced Field Emission

In practice, no metal surface in an accelerator cavity is perfectly flat and clean. As a result, there are large variations in the microscopic surface field which lead to so-called enhanced field emission (EFE). Considerable progress has been made in the past few years in our understanding of the various contributions to EFE. These can be classified into various categories: [3-10]

    (a) Metallic surface roughness due to imperfect machining, scratches, microprotrusions, "tip-on-tip" protrusions

    (b) Metallic dust, microparticles

    (c) Grain boundaries

    (d) Molten craters after breakdown

    (e) Dielectric impurities and layers

    (f) Absorbed gas

    (g) Metal-insulator-vacuum (MIV) or metal-insulator-metal (MIM) layers.

All of these effects can produce emitting sites commonly called "emitters," which can be identified by various surface physics diagnostic techniques. To fix our ideas on a simple problem, let us begin by considering straightforward metallic shapes such as those shown in Figure 2: a sphere above a plane, a cylinder topped by a semi-sphere, and an ellipsoid. For these geometries, F. Rohrbach [11] has calculated the enhancement factor β by which the ideal surface field E is increased to a local microscopic value E_m:

$$\beta = \frac{E_m}{E} \quad . \tag{9}$$

If we assume that the emitter has an effective area A_e, the resulting field emitted current I_F can be derived from Eq. (8) as follows:

$$I_F = \frac{1.54 \times 10^{-6} \times 10^{4.52\phi^{-0.5}} A_e \beta^2 E^2}{\phi} \; \exp \left(-\frac{6.53 \times 10^9 \phi^{1.5}}{\beta E} \right) \; \text{A} \; . \tag{10}$$

The numerical value of β for a particular surface can then be obtained from the knowledge of I_F, E and ϕ by plotting I_F/E^2 versus $1/E$ on semilog paper, which is called a Fowler-Nordheim plot. We notice that the β value, the slope of the line, is given by

$$\frac{d(\log_{10} \; I_F/E^2)}{d(1/E)} = -\frac{2.84 \times 10^9 \; \phi^{1.5}}{\beta} \quad . \tag{11}$$

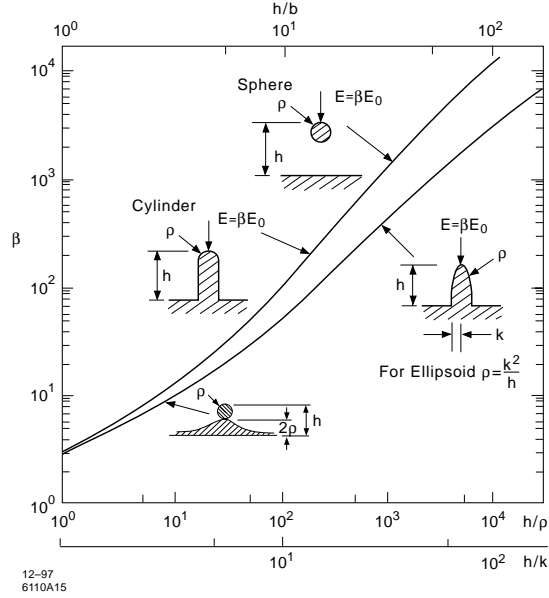The intercept of the line with the $\log_{10} I_F/E^2$ axis, i.e.

4

Figure 2: Field enhancement factor β for idealized metallic microprotrusion geometries (sphere above plane, cylinder topped by semi-sphere, and ellipsoid), plotted vs. h/ρ or h/k (from Rohrbach [11]).

$$\log_{10}\ (I_F/E^2)_{E\to\infty} = \log_{10}\left[\frac{1.54\times 10^{-6}\ A_e\beta^2\ 10^{4.52\phi^{-0.5}}}{\phi}\right],\qquad (12)$$

enables one to calculate the value of A_e.

2.3 Electron Field Emission for RF Fields

If we assume that the microscopic electric field on a metal surface is of the form $E_0\sin\omega t$, the average field emission current can be calculated by time-averaging of Eq. (10):

$$\bar{I}_F = \frac{1}{T}\ \int_0^T\ I_F(t)dt$$

$$= \frac{1.54\times 10^{-6}A_e\beta^2 E_0^2 10^{4.52\phi^{-0.5}}}{\phi}\frac{2}{T}\int_0^{\frac{T}{4}}\sin^2\omega t\exp\left(-\frac{6.53\times 10^9\phi^{1.5}}{\beta E_0\sin\omega t}\right)\,dt\ ,$$

where T is the period of the rf field.

5

The integration can be solved approximately. The field-emitted current for an alternating field can then be expressed as

$$\overline{I}_F \;=\; \frac{5.7 \times 10^{-12} \times 10^{4.52\phi^{-0.5}} \, A_e \, (\beta E_0)^{2.5}}{\phi^{1.75}}$$

$$\times \exp\left(-\frac{6.53 \times 10^9 \times \phi^{1.5}}{\beta E_0}\right) \quad \mathrm{A}, \tag{13}$$

where E_0 is the amplitude of the sinusoidal macroscopic surface field in V/m, β is the enhancement factor as before, and $\overline{I}_F$ is the average field-emitted current in amperes from an emitting area A_e in m^2. Similarly to Eq. (11), we can plot I_F/E^2 versus $1/E$ on semilog paper, and β can be obtained from the slope of the line given by

$$\frac{d(\log_{10} \, I_F/E^{2.5})}{d(1/E)} \;=\; -\, \frac{2.84 \times 10^9 \, \phi^{1.5}}{\beta} \quad . \tag{14}$$

2.4   Field Emission Experimental Results

A large number of experiments have been done over the past years which give typical values for β in the range between 40 and 100. These values as well as the absolute values of I_F can change as a function of time during rf process-ing of a given rf structure, indicating that the quality of the surface and the properties of the emitter(s) are modified. Interestingly, after many hours of processing and breakdown, the metallic microprotrusions observed with a scan-ning electron microscope exhibit ragged shapes (craters and drops of molten copper) which can at best explain β's between 5 and 10 unless, as mentioned above, one assumes multiplicative effects of so-called "tip-on-tip" protrusions ($\sim \beta_1\beta_2$) or other surface physics phenomena such as the presence of absorbed gas, dielectric layers, metal-insulator-vacuum (MIV) or metal-insulator-metal (MIM) effects. In practice, the FE current generally becomes measurable (on the order of a few μA peak) when the local microscopic field exceeds a few GV/m. With a typical β of 50, this corresponds to an applied macroscopic surface field of roughly 40 MV/m, and, in a common disk-loaded accelerator structure (see below), to an axial accelerating field of about 20 MV/m. Because of the exponential growth of I_F vs. E, the field emitted current increases very rapidly with gradients above these values. A typical set of Fowler-Nordheim plots for a seven-cavity S-band standing-wave structure is shown in Figure 3.
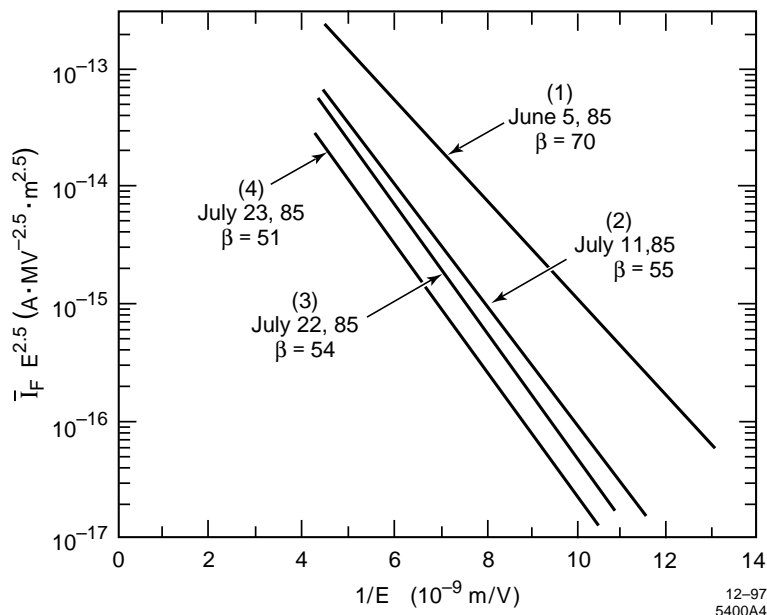
Figure 3: Fowler-Nordheim plots for a seven-cavity S-band structure as a function of time. Line (4) was recorded shortly after using argon scrubbing at a pressure of 10^{-4} to 10^{-5} Torr and subsequent pump-down.

3   Experimental Methods and Set-ups

Aside from computer models, much of the progress made in the US, Japan and Europe in the last ten years in understanding high-gradient rf phenomena has been obtained by testing single or short multi-cavity standing-wave (SW) structures, and longer traveling-wave (TW) accelerator structures. These tests are performed under a variety of configurations and environments but they all have a few features in common: a structure, a pulsed rf power source of some intensity, a vacuum system, and instrumentation. Since electric fields cannot be measured directly without seriously perturbing the experiments, they must be inferred from a precise knowledge of the peak rf power P supplied to the structure, the attenuation τ of the structure, the shunt impedance r_{sw} or r_{TW} which relates the power to the accelerating field, and the relationship between this accelerating field and the peak surface field. The peak surface field generally occurs on disk-edges or nose cones and can be obtained accurately only from computer codes such as SUPERFISH and MAFIA. The accelerating

7

fields are typically given by the expressions

$$E_{SW} = (\frac{P}{l} r_{sw})^{1/2} \text{ for short cavity stacks,} \qquad (15)$$

$$E_{TW} = (1 - e^{-2\tau})(\frac{P}{l} r_{TW})^{1/2} \text{ for constant gradient structures.} \qquad (16)$$

The peak field amplitudes are generally on the order of twice the accelerating fields. The reader is cautioned that the definitions of r_{sw} and r_{TW} are such that it is easy to make errors of a factor of two in the field estimates. Photographs of various cavities and structures are shown in Figure 4. [3]

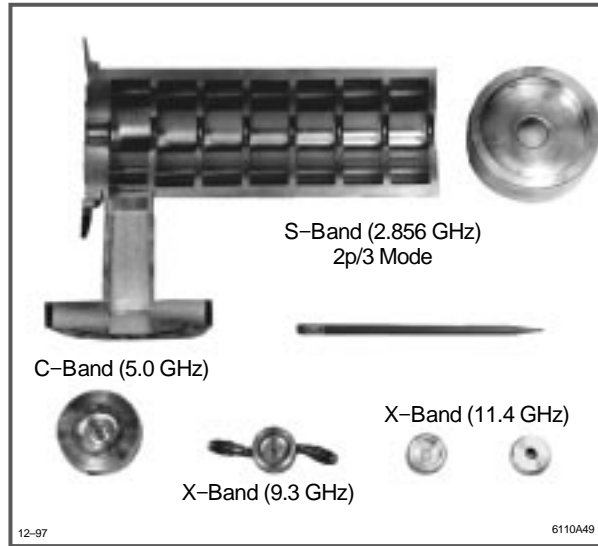Figure 4: Collection of S-band (seven-cavity, $2\pi/3$-mode), C-band and X-band cavities used in high-gradient tests at SLAC in the 1980's.

Regarding instrumentation, experimental set-ups can vary greatly in terms of sophistication and cost. Since field emission, dark current, localized pressure bursts, X-rays and rf breakdown are intimately related, it is necessary to monitor all these phenomena simultaneously. The problem is that field-emitted electrons have very complicated trajectories (see next section) and not all of them are extractable on-axis and measurable externally with spectrometers and Faraday cups. Many of them strike the cavity walls. In some

cases, weakly perturbing probes can be inserted into the cavities, and in general, X-rays can be monitored from the outside. In some cases, it is possible to observe the emission of visible light via a TV camera pointing at the inside of a cavity through a window and a mirror.

In recent years, the increasing availability of X-band (11.424-GHz) power from klystrons in the SLAC Test Lab has made it possible to construct a fairly complete facility called ASTA (Accelerator Structure Test Area),[12] the layout of which is shown in Figure 5. A photograph of ASTA is shown in Figure 6.
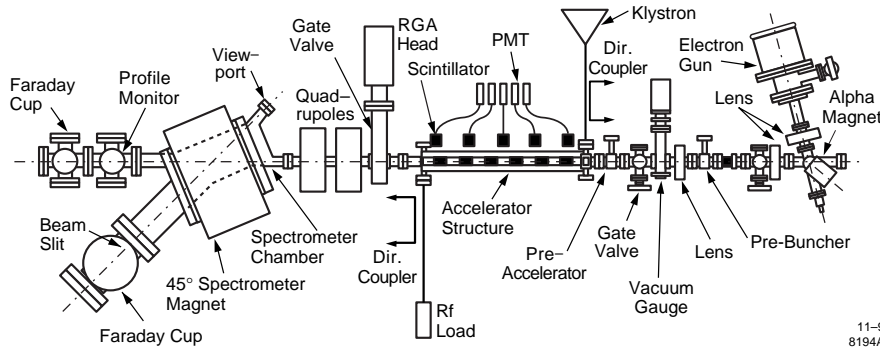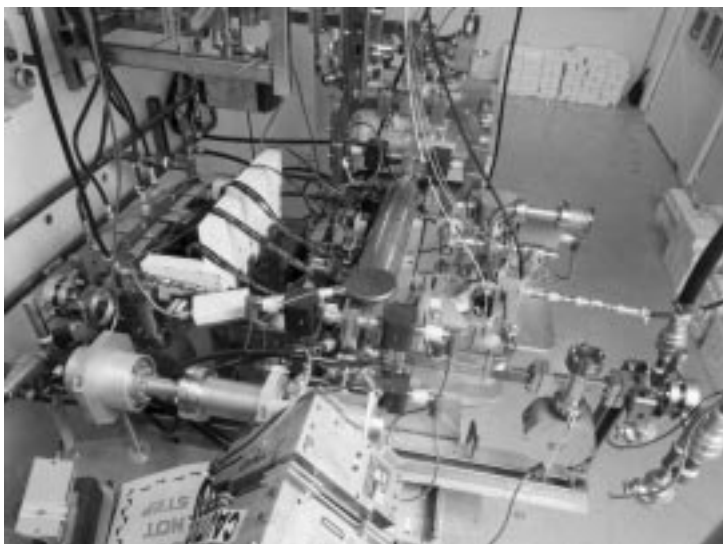

Figure 5: Layout of ASTA (Accelerator Structure Test Area) at SLAC (beam goes from right to left).

This facility enables one to insert various accelerator structures in the middle and study their behavior by means of all the surrounding instrumentation. It is even equipped with an off-axis electron gun and associated injection equipment which allows one to observe controllable accelerated beams. The X-ray measurement devices include scintillators, photomultipliers, pin-hole cameras, ion chambers and dosimeters.

One of the major problems in studying the relationship between surface physics, field emission and rf breakdown is that it is difficult to know exactly the starting conditions of a cavity surface. This is because the number of steps involved in fabricating, cleaning and installing it are complex and not always reproducible. Furthermore, once the tests begin, the conditions inside the structure change and it is difficult to follow exactly what happens to the surfaces. If one stops the tests at some point, one then gets only a cumulative snapshot of whatever events have taken place. Also, the diagnostic surface analysis techniques are hard to apply unless one removes or cuts out a piece of the structure, which then involves an irreversible process. Removable nose cones[13] can circumvent this problem, but they sometimes create difficulties of

9

11–97
8362A1

Figure 6: Photograph of Accelerator Structure Test Area (ASTA) at SLAC.

their own.

SLAC is fortunate to have at its disposal a very strong and well equipped surface physics analysis laboratory, which includes scanning electron microscopes (SEM), auger electron spectroscopy (AES), energy dispersive X-ray analysis (EDAX), X-ray photoelectron spectroscopy (XPS), and others. Copper and other samples (coupons) can be studied before and after tests, and various types of impurities and defects can be analyzed and monitored. Similar work has been done at the University of Geneva, Switzerland, [14] Cornell University, [15] Wuppertal, Germany, [16] and elsewhere (predominantly for superconducting cavities). The suspicion that impurities in crystal boundaries are at least partially responsible for field emission and rf breakdown has motivated KEK researchers to use HIP (hot isostatic pressed) metals (copper or titanium) [17] in a number of their cavities, particularly for their disks. High quality clean room, chemical cleaning techniques, high-pressure high-purity water jets, and other methods are all part of the artillery employed in this field. As will be seen later in this article, much progress has been made but no definite set of recipes has yet been determined for obtaining totally predictable results.

10

4 Prebreakdown Stage: Dark Current and Radiation

Dark current and X-ray radiation, together with outgassing and temperature changes are the first observable phenomena which appear under high-gradient operation before a structure begins actually to break down. For this reason, they are considered as "prebreakdown" phenomena even though the exact sequence of events leading to breakdown is not entirely clear. We will now briefly examine the manifestation of dark current and X-ray radiation under these conditions.

4.1 Dark Current

When FE electrons are first generated in an accelerator structure, they come preferentially from high-field regions such as disk-edges, but at relatively low absolute fields, their trajectories and the points where they hit a cavity wall are fairly random. Together with secondary electrons emerging from impacted areas, they end up producing the equivalent of an electron gas in each cavity. Figure 7, which illustrates this effect, is the result of a calculation performed by R. Parodi of INFN, Genoa,[18] applying his computer program NEWTRAJ to the geometry of a SLAC short S-band structure. When the electron, which is accelerated by the rf field, strikes the cavity wall at some impact point, a secondary or backscattered electron is generated, whose starting condition depends on the energy of the impact electron, its impact angle and the secondary emission coefficient of the surface.
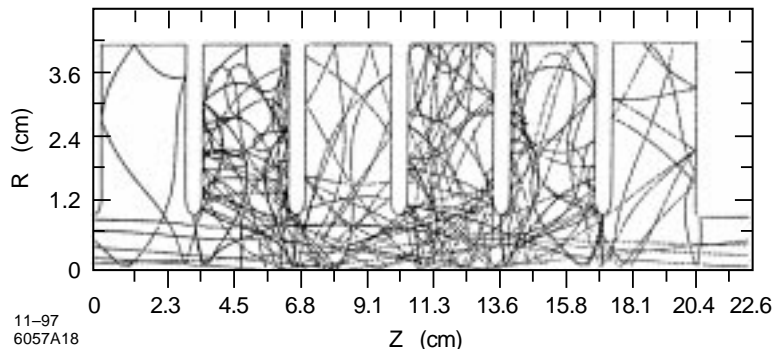

Figure 7: Field-emitted electron trajectories plotted for S-band structure by means of NEW-TRAJ computer program (courtesy of R. Parodi).

The threshold of normalized electric field ($\mathcal{E}_0 \equiv eE_0/mc^2$) for capture in a

velocity-of-light structure can by expressed as [19]

$$\mathcal{E}_0/k = \frac{1}{2}[(p_0^2 + 1)^{1/2} - p_0] \quad , \tag{17}$$

where $k = 2\pi/\lambda$ is the propagation constant and p_0 is the initial normalized momentum. For field-emitted electrons with near zero initial momenta ($p_0 = 0$), axial capture and cumulative acceleration occur when the accelerating gradient is raised above a critical value E_c given by

$$E_c = 1.6/\lambda \qquad \mathrm{MV/m} . \tag{18}$$

The problem with this captured current is that it can build up along each structure and from structure to structure. Captured electrons parasitically absorb rf energy, cause increased radiation, backgrounds, noise in instruments, and possibly wakefields. Fortunately, there is recent evidence [20] that in a practical machine the captured electrons are to a large extent deflected transversely and eliminated by the focusing quadrupole array along the linac (whose strength scales with distance from the injector, unlike the energy of the locally captured particles). Hence, the risk of these electrons reaching the end of the linac and the final focus is considerably decreased, whereas local radiation and noise remain a problem. Clearly, the $1/\lambda$ dependence of E_c favors high rf frequency linacs for which the capture threshold is higher.

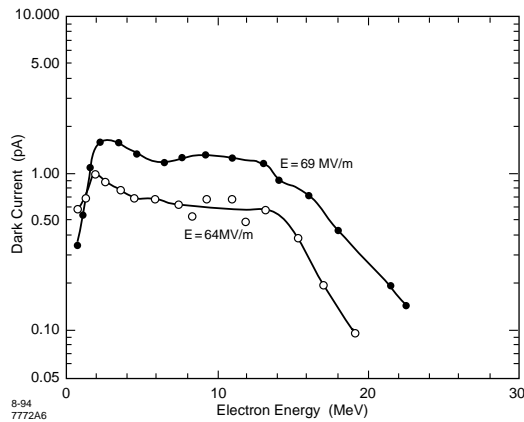Figure 8 shows the momentum analyzed average dark current measured at

Figure 8: Average dark current at a fixed spectrometer slit width as a function of electron energy for two gradients in a 75-cm traveling-wave 11.424-GHz constant-impedance accelerator section.

12

two different gradients for a TW 75-cm constant-impedance accelerator section tested in the ASTA facility. The collimator slit at 45° for the spectrometer (see Figure 5) was set at 5.3 mm. The relatively flat top of the two curves indicates that the dark current was captured fairly uniformly along the structure.

Note that the effects described here so far occur in velocity-of light structures. If the rf frequency is changed slightly, the capture is modified. For example, some very interesting phenomena were observed when a 30-cavity X-band TW constant-impedance structure was high-power tested. Figure 9 shows the rf pulse shapes and dark currents for three different pulse rise times. It shows that for a steep rise time of about 10 ns (Figure 9a), which probably causes an upward frequency shift of several tenths of a megahertz (and a slight overshoot in amplitude), the capture is significantly increased. When the frequency shift subsides after about a filling time (26.5 ns), the dark current subsides accordingly. The effect becomes less pronounced as the rise time increases to about 15 ns (Figure 9b) and disappears completely for a rise time of about 20 ns (Figure 9c). This effect can be explained by the fact that the higher frequency leads to a lower phase velocity which causes more electrons to be captured. This hypothesis was verified by changing the rf drive frequency for the entire pulse (Figure 10) and observing the increase in dark current at a fixed value of average E_{acc} (77 MV/m).
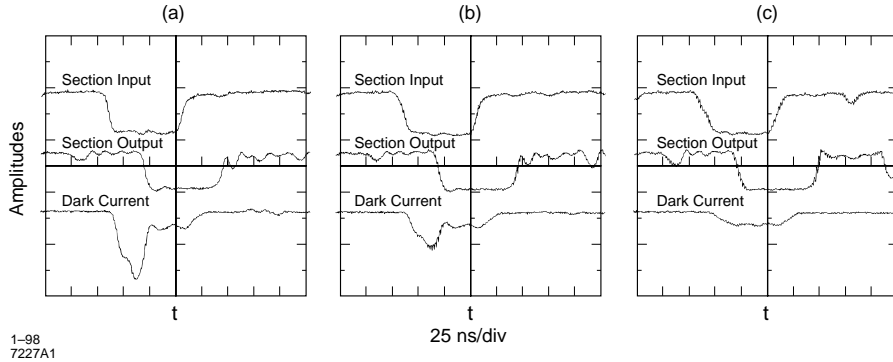

Figure 9: Pulse shapes of section input, output and dark current for three different rise times of the rf pulse for a 30-cavity X-band TW section test.
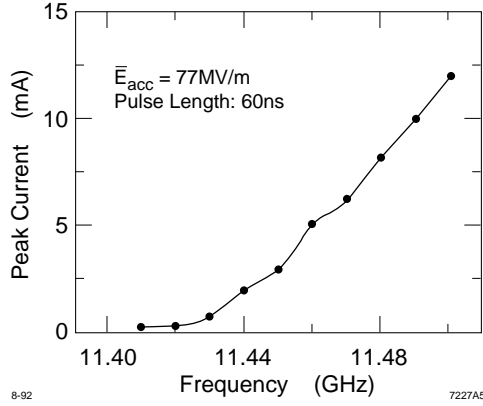
13

Figure 10: Peak dark current as a function of rf frequency.

4.2 Radiation

From the trajectories shown in the previous paragraph, it is clear that the electrons hitting the walls of a structure will produce X-rays in all directions. This radiation depends on the impinging electron energy spectrum and on how much copper it must traverse before reaching the instrumentation. Three examples are shown below. The first one (Figure 11) shows the average X-ray dosage distribution around a seven-cavity S-band accelerator section with a maximum surface field of 300 MeV/m. The dosage obtained with ion chambers is measured in megarems-per-hour and is very large.
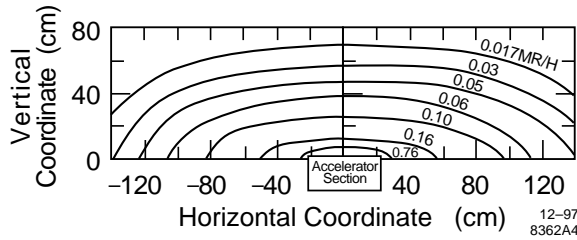

Figure 11: Average X-ray dosage distribution in megarads/h around S-band (seven-cavity, $2\pi/3$ mode) accelerator section (300 MV/m surface field, 2.5 μs pulse length, 120 Hz repetition rate).

The second example, shown in Figure 12, is the image of a klystron cavity

14

with nose cones, taken with a 1/2 mm pin-hole camera, Fuji imaging plate, laser scanner and computer digitizer.[21] The darker areas indicate, as expected, that the radiation comes predominately from the high-field nose cones.

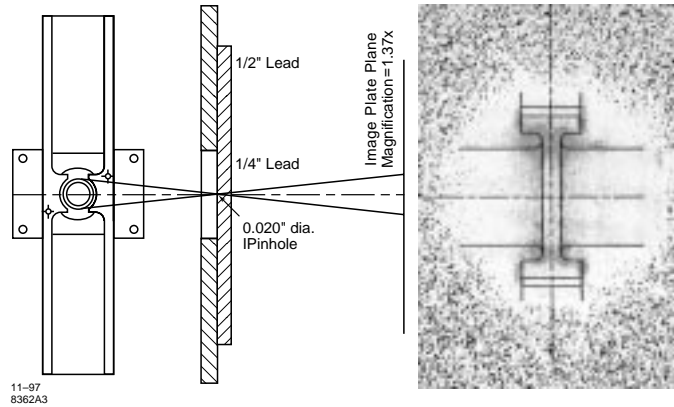Figure 12: X-ray image for a X-band klystron output cavity at high power test (courtesy of R. Fowkes).

The third example, illustrated in Figure 13,[22] shows the radiation dosage alongside a 1.8-m-long quasi-constant-gradient accelerator section tested in ASTA at two different average gradients.[23] The radiation was measured with five sodium iodide crystal scintillators, coupled to optical fibers and photomultiplier amplifiers. In all these tests, it was observed that the radiation (as well
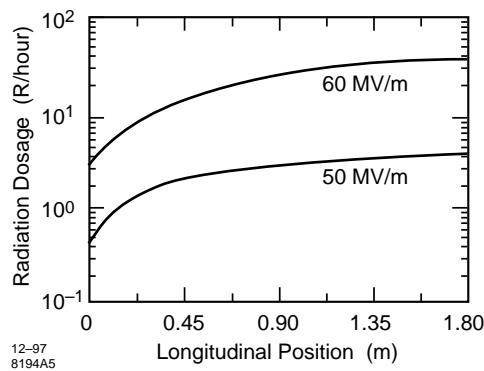

Figure 13: Radiation dosage along a 1.8-m X-band quasi-constant-gradient accelerator section for two different average gradients.

15

as the dark current) is very steady and repeatable from rf pulse to pulse, and constant within each pulse, once steady-state has been reached after the appropriate number of filling times. Only when rf processing (see below) causes changes in surface quality, can one observe significant changes in the dark current and radiation.

5   Experimental Observations and Analysis of RF Breakdown

5.1   Basic Phenomenology

Whereas normal FE is a stable, steady-state phenomenon, rf breakdown is an instability which leads to a "runaway" condition. There is very little doubt that FE is the initial cause of rf breakdown, but the exact sequence of events between initial rf processing (predominantly outgassing) and ultimate processing, when structures are pushed to their limit, is not totally clear. Above a microscopic field of a few GV/m, j_{FE} can approach 10^{11} A/m^2. Above this level, the ri^2 Joule losses in an emitter can heat it in a few or tens of nanoseconds to the point of vaporizing some or all of its contents (gas, metal, etc.).[24] The positive ions, produced by ionization of the neutral gas by the FE electrons, can form a sheath along the emitter and/or impinge on it, precipitating further increased FE, more ions, eventual explosion or meltdown, metal droplets, and expanding damage in the form of craters. Experimental evidence for these phenomena is corroborated by the observation of visible sparks, instantaneous increase of the emitted current by a factor of about 40, detection of puffs of gaseous H, CH$_4$, H$_2$O, CO and CO$_2$, X-ray bursts, and collapse (within the rf pulse) of the cavity fields, manifested by a reflection of the incident rf power.

We shall come back to these observations in some greater detail after discussing the observed rf frequency dependence of rf breakdown.

5.2   RF Frequency Dependence

As discussed earlier, rf breakdown tests have been performed all over the world for about 40 years. One of the first authors who tried to give an explanation and a criterion for the dependence of rf breakdown on frequency was W.D. Kilpatrick.[25]

The Kilpatrick criterion was based on the idea that breakdown happens when regular FE is enhanced by a cascade of secondary electrons ejected from the surface by ion bombardment. Assuming a linear dependence of secondary emission of electrons upon maximum ion energy, an expression for the breakdown or "sparking" threshold was obtained empirically from early experimental data gathered in the 1950's, as

$$WE^2\exp(-1.7 \times 10^5 E^{-1}) = 1.8 \times 10^{14}, \tag{19}$$

where W is the maximum possible ion energy in eV and E is measured in V/m. The maximum energy of an ion of mass M_0 and charge e, calculated from a relatively large gap of parallel plates and taking into account the transit time, was found to be

$$W = \frac{0.153 \, e \, E^2}{M_0 \pi \, f^2} \quad , \tag{20}$$

from which the Kilpatrick criterion was derived as

$$f = 1.64 \, E^2 \exp(\frac{-8.5}{E}) \quad , \tag{21}$$

with f measured in MHz, E in MV/m and the ion assumed to be hydrogen. Inverting expression (21), we then obtain

$$Ee^{-4.25/E} = 24.7 \, [f(\text{GHz})]^{1/2} \quad \text{MV/m} . \tag{22}$$

Much more recent experiments performed since about 1985 on a variety of single copper cavities and two short resonant accelerator sections[3] indicate that the maximum surface fields attainable after aggressive rf processing (i.e., where the incident power is driven up without fear of producing surface melting and craters) are about 310 MV/m at 2.856-GHz and 500 MV/m at 11.424-GHz. There are no available experimental data for full-length structures. Taking into account all existing results, the most conservative fit for the maximum surface field is given by

$$E = 220 \, [f(\text{GHz})]^{1/3} \quad \text{MV/m} . \tag{23}$$

Note that this expression is empirical and at this point in time has no solid theoretical foundation. Indeed, the fact that equation (13) shows no frequency dependence means that any explanation for equation (23) must come from some other physical cause (see discussion below). Note that the predictions made by the Kilpatrick criterion yield values that are 6 or 7 times lower than those obtained with cavities built in the past ten years or so. This is not surprising for a number of reasons. First of all, the early experimental data that went into the above empirical equation (19) have been superseded by much higher quality cavities and structures. Second, the formula for W was based on a gap of parallel plates which is quite different from the condition inside rf cavities with rounded disks. Finally, the multiplicative effect of W in equation (19) assumed that the avalanche of secondary electrons by ion

collisions was the dominant cause of rf breakdown. What is now much more likely is that the breakdown observed in accelerator cavities is a single-electrode effect where the ions do not have the time to move across a gap. Rather, if the ions play a role, it is because they result from FE electrons ionizing small bursts of surface-emitted gas in close vicinity of the disks. As a result, a positively charged sheath is formed near the surface which greatly enhances the localized microscopic electric field.[26] Why this effect might show a frequency dependence is not clear. Perhaps the number of ions in the sheath is somehow inversely proportional to some fractional power of the frequency ($\sim f^{-n}$), or for a given number of ions, the sheath can come nearer the surface at lower frequency, thereby precipitating breakdown at a lower microscopic field. These are just conjectures.

5.3 RF Processing and RF Breakdown

We will now try to summarize the chronological sequence of steps and processes to which a typical cavity or structure is submitted from the time it is fabricated, cleaned, installed and connected to an rf source and before it is ready for steady high-gradient operation:

(a) The structure is typically vacuum baked either in a baking furnace at $350° - 500°$C, or in situ at $\sim 200°$C for a few days.

(b) The structure is then pumped down to $\sim 10^{-8}$ Torr.

(c) Pulses of gradually increasing rf power (on the order of μseconds in duration or less) are carefully applied to the structure.

(d) As the structure walls heat up and FE appears, outgassing begins and, if an RGA is available, its readouts (see Figure. 14(a)) exhibit a strong H line (from hydrogen adsorbed during brazing), and weaker C, CH, CH_2, CH_3, CH_4, HO, HO_2, N_2, CO, and CO_2 lines.

(e) Depending on how aggressively one pursues the rf processing, one can occasionally produce an rf breakdown event as the power level increases. One can program the system so that when the pressure increases to a certain level or the rf signal reflected back to the rf source (see below) reaches a certain threshold, the rf power is temporarily tripped off, then turned back on and ramped up again. Because one does not know exactly what the state of outgassing and clean-up of impurities inside a structure is at any given time, rf processing is still an art more than a science. If one is very patient, the ultimate gradient that can be reached may be greater, but the time required to obtain it may be long, and sometimes unacceptably long (somewhere between tens and hundreds of hours).

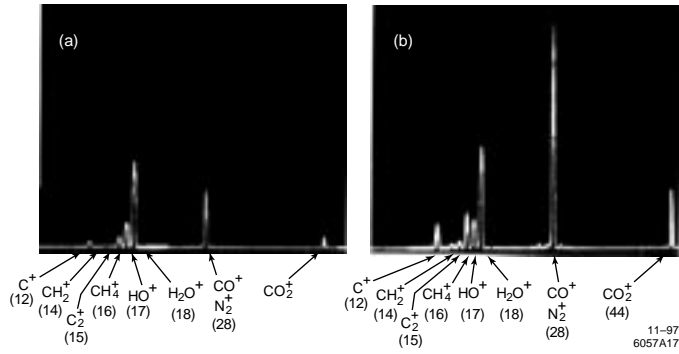Figure 15 is a record of the rf processing of the 1.8-m structure mentioned

Figure 14: Residual gas analyzer display during rf processing of S-band, two-cavity structure, (a) before breakdown, and (b) immediately after breakdown.

earlier. It took 30 hours over a two-day period to reach an average accelerating gradient of 50 MV/m. Higher levels could not be reached because of rf power limitations.
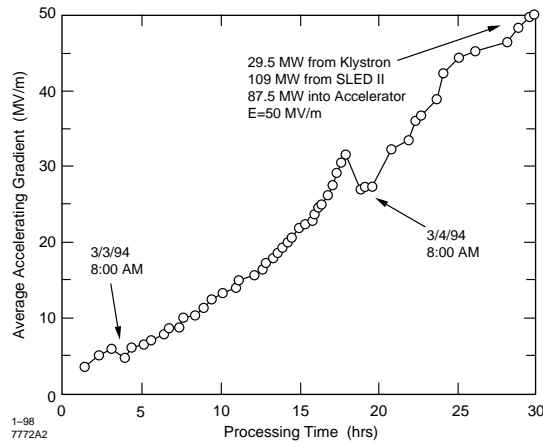

Figure 15: RF processing schedule for the 1.8-m X-band quasi-constant-gradient accelerator section.

(f) As the rf field inside a structure is increased and a breakdown event is triggered, several effects take place almost simultaneously:

19

i. The reflected rf pulse jitters violently, indicating that the fields inside the structure have collapsed (see Figure 16).

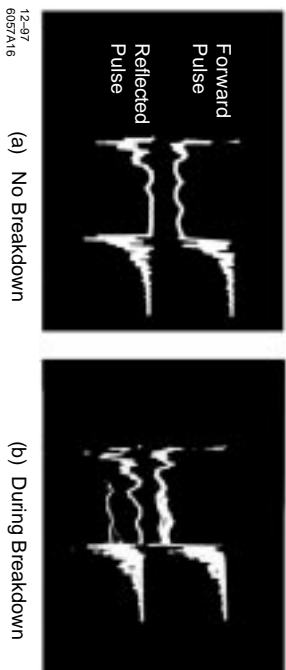(a) No Breakdown   (b) During Breakdown

Figure 16: Forward and reflected rf waveforms: a) normal, b) during breakdown for a SW X-band accelerator section.

ii. If a window is available to look inside the structure, sparks are generally visible close to the high-field areas, indicating that some gas discharge and ionization are taking place.

iii. The RGA readouts show a sudden surge illustrated in Figure 14(b), and if the breakdown is made to persist, the pressure in the structure may rise to 10^{-7} or even 10^{-6} Torr.
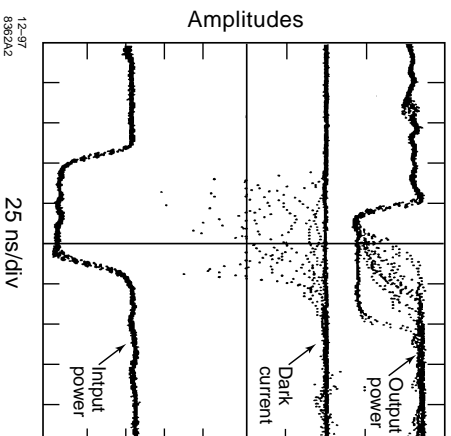

Figure 17: Input and output rf waveforms and dark current display obtained from the high power test of a 75-cm X-band constant-impedance accelerator section.

20

iv. Whatever steady FE current is present before breakdown, this current instantaneously jumps up by a factor of 30-40, and the resulting X-ray radiation increases accordingly (see Figure 17). For the rf pulse lengths available for these experiments, it appears that the time onset of breakdown within these pulses is fairly random once the cavity or structure has reached the steady state. The rf breakdown seems to occur within a few nanoseconds or tens of nanoseconds during which localized outgassing and/or melting of the copper surface takes place.

v. This breakdown pattern repeats itself until one reaches an asymptotic field beyond which progress does not seem possible. With newly installed structures which have been processed once and then let up to clean air, reprocessing can take several hours before the highest gradient is again reached. If the structure is not supplied with rf but left under good vacuum (10^{-8} Torr) for several days or over months (like for example the SLAC linac), reprocessing can be done in a few minutes or a fraction of an hour.

vi. With aggressive rf processing, the overwhelming evidence is that localized copper melting takes place, as illustrated in Figure 18[27] and Figure 19[13]. The process is obviously irreversible, but our Fowler-Nordheim plots at SLAC show that the global microscopic field enhancement factor β after the craters and copper droplets are formed does not get much worse than 50, even if there are many such crater formations.

vii. That melting takes place is not surprising. Consider a surface area from which a large FE current density j emerges and dissipates heat from ohmic loss $\bar{j}^2 \rho$ where ρ is the resistivity of the medium. If we assume to first order that this heat does not have the time to be conducted away, it will raise the temperature of the volume by $\Delta T(^\circ\text{C})$ in a time

$$\Delta t = \frac{4.18 \times 10^6 M C \Delta T}{\bar{j}^2 \rho} \tag{24}$$

where M is the density in gram/cm^3, C is the heat capacity per gram, and ρ is measured in ohms-cm. As it turns out, the time to reach the melting point of the metal does not depend very much on which metal is considered (in agreement with some experimental results[28]) and is roughly equal to

$$\Delta t = \frac{2 \times 10^9}{\bar{j}^2} \quad \text{seconds} \quad . \tag{25}$$

If for example $\bar{j} = 3 \times 10^8$ A/cm^2, then $\Delta t \sim 22$ nsec, a result which seems to be quite consistent with all our observations and those of researchers at other laboratories.
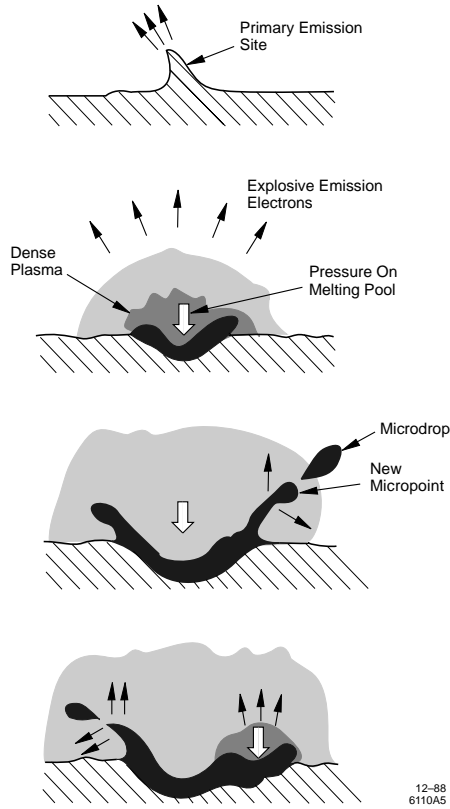
Figure 18: Development of surface damage in the case of breakdown initiated by Explosive Electron Emission (EEE)[27].

viii. Note that the Fowler-Nordheim plots which yield the values of β are probably determined by the worst single (or few) emitters in a surface. The point at which a Fowler-Nordheim line intercepts the y-axis is proportional to the emitting area. However, the problem of extracting a meaningful number for this area is obscured by the difficulty of measuring the exact value of I_F above, since the shapes of the cavities and their field configurations allow us to extract only a small fraction of the electrons. Furthermore, if a structure is long, the current that comes out at the ends is cumulative and depends strongly on whether the accelerating field is below or above the capture gradient (see equation 18 above) and the exact rf frequency at which one operates, as discussed earlier.
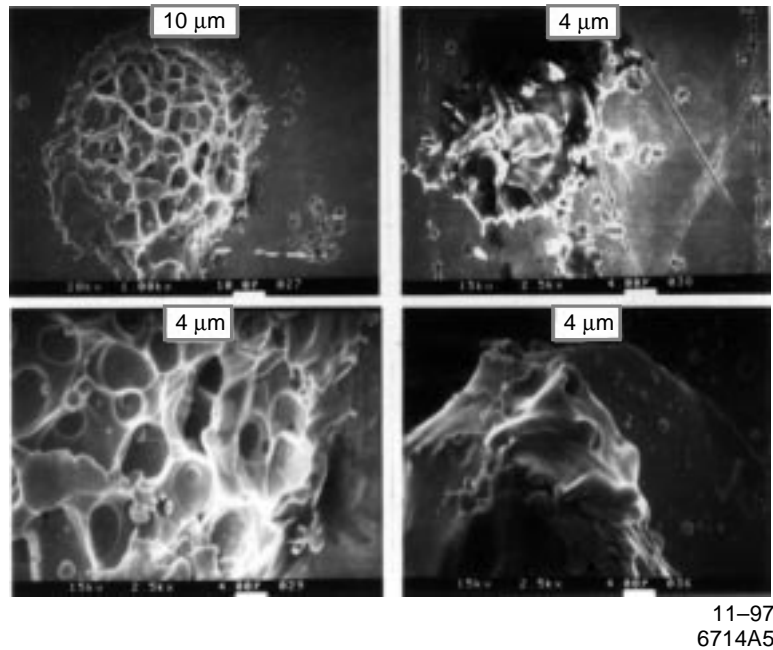
10 μm 4 μm 4 μm 4 μm

11–97
6714A5

Figure 19: Scanning electron microscope pictures of damaged sites on nose cone of S-band cavity after aggressive rf processing and breakdown.

ix. The fabrication and cleaning procedures can also strongly affect these ultimate current densities, as shown by the work done at KEK,[29] summarized in Figure 20 for three different S-band SW cavities. Indeed, cavities II and III in Figure 20 show an order of magnitude lower current than cavity I. Also, Figure 21, which gives RGA spectra for cavities I and II for two levels of rf processing each, shows that the corresponding partial pressure of CO and CO_2 can be considerably reduced with the appropriate precautions.
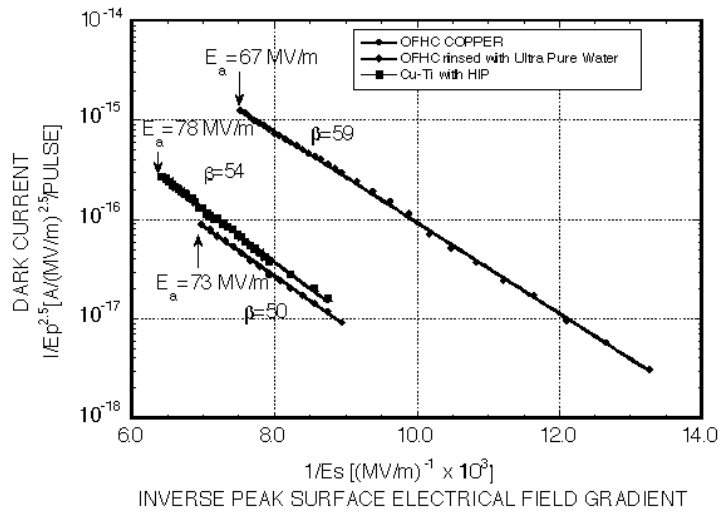
Figure 20: Fowler-Nordheim plots for three different cavities: I) Conventional OFHC copper, class 10,000 environment. II) OFHC copper, cavity rinsed with ultra pure water and assembled in class 1 clean room. III) Composite cavity, disk-edges made out of hot isostatic pressed (HIP) titanium (courtesy of H. Matsumoto).
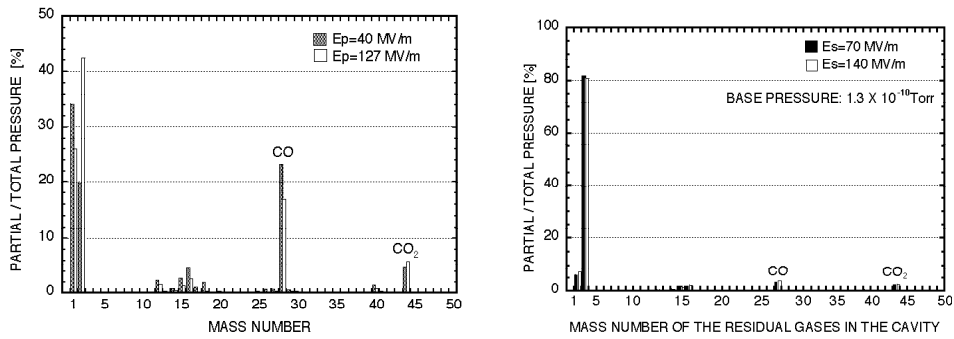

Figure 21: Residual gas spectra for cavity I (left spectrum) and for cavity II (right) for two levels of rf processing (courtesy of H. Matsumoto).

24

6   Conclusions

In this article, we have attempted to review the current status of knowledge on the subject of field emission and rf breakdown in high-gradient room-temperature accelerator structures. The reader will have noticed that this field of research is very dynamic, that continuous progress is being made, and that some basic and practical questions still remain to be answered. A brief summary is presented below.

1. The basic phenomenon of electron field emission as a source of dark current and as a trigger of rf breakdown in accelerator structures is well-established. What is still missing is a deeper understanding of what exactly makes up the value of the enhancement factor β and how it is to be correlated with, and ultimately predicted from an observable surface condition. When many similar surface emitters are present, is the measured β the result of the sum of these emitters or is it always dominated by one of them?

2. In the fairly well-established chain of events that leads to rf breakdown, is the sudden burst of gas and ion formation the ultimate enhancer of the local microscopic field which triggers a breakdown event?

3. Why does the surface field at which breakdown occurs depends on rf frequency when the classical Fowler-Nordheim expression for field emission is independent of frequency? Is this empirical frequency dependence real, or is it perhaps influenced by the fact that the rf pulse lengths used in experiments are generally shorter at higher frequency? On the other hand, in those experiments where the pulse length was varied at a given rf frequency, why is it that pulse length, admittedly over a small available range, did not have much of an effect on the breakdown threshold? Or perhaps, is the frequency dependence just due to the fact that higher frequency structures are smaller and therefore contain fewer defects and impurities?

4. Finally, from a practical point of view, what must be done to limit dark current and push the threshold of breakdown to the highest possible level? It is clear that every step in the fabrication, cleaning and installation of an accelerator structure can affect these two parameters: i.e., the raw material, machining practices, brazing, cleaning methods, environmental conditions during assembly and installation, in situ baking, the number of impurities per cm^2 left on the surface before the structure is pumped down, and the ultimate rf processing schedule. What is not clear is which of these steps are more crucial than others. Indeed, building an accelerator structure is a complicated and costly process, and eliminating unnecessary steps is very important, particularly for machines that may require thousands of accelerator sections. Some very interesting research still lies ahead.

References

1. R.H. Fowler and L. Nordheim, Proc. Roy. Soc. A119, 173-81, 1928.
2. R.H. Good and E.W. Müller, Field Emission, in "Handbuch der Physik," Springer Verlag, Berlin, 21, 176-231, 1956.
3. G.A. Loew and J.W. Wang, RF Breakdown Studies in Room Temperature Electron Linac Structures, SLAC-PUB-4647, 1988.
4. R.V. Latham, Prebreakdown Electron Emission Processes, in Proc. 12th Int. Symp. on Discharges and Electrical Insulation in Vacuum, 1986.
5. K.H. Bayliss and R.V. Latham, Proc. Roy. Soc., A 403, 285-311, 1986.
6. N.S. Xu, The Physical Origin of Prebreakdown Electron 'Pin-Holes', in "High Voltage Vacuum Insulation," R.V. Latham ed., London, Academic Press, 1995.
7. C.S. Athwal, et al., IEEE Trans. Plasma Sci., PS-13(5), 226-229, 1985.
8. M. Luong, et al., Role of Adsorbates on Current Fluctuations in DC Field Emission, in Proc. 7th Workshop on RF Superconductivity, Gif-sur-Yvette, France, (also Saclay report 96 080/1).
9. M. Jimenez, et al., J. Phys., 27, 1038-45, 1994.
10. B. Bonin, et al., Field Emission Studies at Saclay, in Proc. 6th Workshop on RF Superconductivity, R. Sundelin, ed., CEBAF, 1993.
11. F. Rohrbach, CERN 71-28, October 1971.
12. A.E. Vlieks, et al., Accelerator and RF System Development for NLC, presented at 1993 Part. Accel. Conf., Washington, DC, SLAC-PUB-6148, 1993.
13. G.A. Loew and J.W. Wang, Progress Report on High-Gradient RF Studies in Copper Accelerator Structures, presented at 14th Int. Symp. on Discharges and Electrical Insulation in Vacuum, Santa Fe, NM, Sept., 1990, SLAC-PUB-5320.
14. P. Niedermann, Ph. D. Thesis No. 2197, University of Geneva, 1986.
15. H. Padamsee, Advances in Basic Understanding of Field Emitters and HV conditioning, presented at RF96, Japan, 1996.
16. N. Pupeter, et al., Appl. Surface Sci. 94/95, 94-100, 1996.
17. H. Matsumoto, et al., Application of Hot Isostatic Pressing (HIP) for High-Gradient Accelerator Structures, presented at IEEE Particle Accelerator Conf., May 1991.
18. Calculations carried out by R. Parodi, INFN, Genoa, Italy, in collaboration with SLAC.

19. R.H. Helm and R. Miller, Particle Dynamics, Chapter B.1.2 of "Linear Accelerators," P.M. Lapostolle and A. Septier, eds., North-Holland, Amsterdam, 1970.
20. S. Takeda, Background and Dark Current Experiment at ATF S-band Linac, presented at 7th Int. Workshop on Linear Colliders, Sept. 29-Oct. 3, 1997.
21. R. Fowkes, SLAC, Private communication, 1996.
22. J.W. Wang, et al., High-Gradient Experiments on NLCTA Accelerator Structures, presented at LINAC96, Geneva, Aug. 1996, SLAC-PUB-7243, 1996.
23. J.W. Wang, et al., High-Gradient Tests of SLAC Linear Accelerator Structures, presented at LINAC94, Tsukuba, Japan, Aug. 1994, SLAC-PUB-6617, 1994.
24. J.W. Wang, RF Properties of Periodic Accelerator Structures for Linear Colliders, SLAC-Report-339, 1989.
25. W.D. Kilpatrick, Rev. Sci. Instrum., 28, 824-826, 1957.
26. J. Knobloch, Advanced Thermometry Studies of Superconducting RF Cavities, CLNS Thesis 97-3, Cornell University, 1997.
27. G.A. Mesyats, IEEE Trans. Electrical Insulation, EI-18 (3), 1983.
28. E. Tanabe, Breakdown in High-Gradient Accelerator Cavities, presented at LINAC84, Darmstadt, Germany, June 1984.
29. H. Matsumoto, Dark Current, presented at 18th Linear Accelerator Conf., Geneva, Aug. 1996.